Ultrathin Carbon Nanosheets for Highly-efficient Capacitive K-ion and Zn-ion Storage

Yamin Zhang [b, c], Zhongpu Wang [b], Deping Li [a, b] *, Qing Sun [b], Kangrong Lai [c], Kaikai Li [a], Qunhui Yuan [a], Xingjun Liu [a] and Lijie Ci [a, b] *

[a] State Key Laboratory of Advanced Welding and Joining, School of Materials Science and Engineering, Harbin Institute of Technology, Shenzhen, 518055, China

[b] Research Center for Carbon Nanomaterials, Key Laboratory for Liquid-Solid Structural Evolution & Processing of Materials (Ministry of Education), School of Materials Science and Engineering, Shandong University, Jinan, 250061, China

[c] Department of Physics, Changji University, Changji 831100, China

Address correspondence to **cilijie@hit.edu.cn**; lideping@hit.edu.cn

Abstract

Porous carbon has attracted extensive attentions as the electrode material for various energy storage devices considering its advantages like high theoretical capacitance/capacity, high conductivity, low cost and earth abundant inherence. However, there still exists some disadvantages limiting its further applications, such as the tedious fabrication process, limited metal-ion transport kinetics and undesired structure deformation at harsh electrochemical conditions. Herein, we report a facile strategy, with calcium gluconate firstly reported as the carbon source, to fabricate ultrathin porous carbon nanosheets. The as-prepared Ca-900 electrode delivers excellent K-ion storage performance including high reversible capacity (430.7 mAh g^{-1}), superior rate capability (154.8 mAh g^{-1} at an ultrahigh current density of 5.0 A g^{-1}) and ultra-stable long-term cycling stability (a high capacity retention ratio of ~81.2% after 4000 cycles at 1.0 A g^{-1}). Similarly, when being applied in Zn-ion capacitors, the Ca-900 electrode also exhibits an ultra-stable cycling performance with ~90.9% capacity retention after 4000 cycles at 1.0 A g^{-1}, illuminating the applicable potentials. Moreover, the origin of the fast and smooth metal-ion storage is also revealed by carefully designed consecutive CV measurements. Overall, considering the facile preparation strategy, unique structure, application flexibility and in-depth mechanism investigations, this work will deepen the fundamental understandings and boost the commercialization of high-efficient energy storage devices like potassium-ion/sodium-ion batteries, zinc-ion batteries/capacitors and aluminum-ion batteries.

Key words: *In situ* self-template fabrication strategy, Ultrathin porous carbon nanosheets, Potassium-ion batteries, Zinc-ion hybrid capacitors, Capacitive energy storage

1. Introduction

Lithium-ion batteries (LIBs), as the representative secondary battery systems, have been triumphantly used in electric vehicles, portable electronics, and smart grids[1, 2]. However, with the development of technologies, the dependence on LIBs has led to the rising cost and reducing availability of lithium resources in the crust[3]. Therefore, it is urgent to find alternatives to LIBs. Sodium-ion batteries (SIBs) have become the focus of attention because of their earth-abundant inherence and similar electrochemical properties to LIBs[4, 5]. Nevertheless, sodium ions are difficult to be reversibly inserted into the graphite anode, limiting its commercialization prospect.

Potassium-ion batteries (PIBs), rooting in competitive crust reserves (~15000 ppm) and feasible K-ion insertion/extraction in commercial graphite electrode, are attracting enormous attentions. Besides, the redox potential of K^+/K (-2.93V) is lower than that of Na^+/Na (-2.71V), and close to Li^+/Li (-3.04 V), indicating that PIBs can work within a high voltage platform and deliver a high energy density[6, 7]. In addition, in organic solvent electrolytes, such as propylene carbonate (PC), K^+/K (-2.88 V) exhibits the lowest redox potential compared to Li^+/Li (-2.79 V) and Na^+/Na (-2.56 V)[8, 9]. Despite a larger ionic radius of K-ion, owing the weak Lewis acidity of K-ion, the radius of solvated K-ion is the smallest as compared to Li-ion and Na-ion, which leads to higher ionic conductivity and greater mobility in the electrolyte[10]. Meanwhile, the formation enthalpy of KC_8 (-27.5 kJ mol^{-1}) is lower than that of LiC_6 (-16.5 kJ mol^{-1})[11], which means that K ions are easier to insert into graphite. Above all, the K-ion transportation in the electrolyte is a kinetic-favorable process. However, the diffusion rate of K-ion in the interior of the electrode is still significantly restricted by its large ionic radius (1.38 Å *vs.* 1.02 Å of Na-ion and 0.76 Å of Li-ion), which will induce severe volume expansion and structure collapse of the electrode material during repeat potassiation/de-potassiation processes[12]. For example, the formation of KC_8 compound endures a ~61% volume expansion, which is six times of the lithiated graphite (LiC_6)[13]. To overcome this obstacle, adjusting the interlayer distance and decreasing the K-ion diffusion distances of carbons could effectively ameliorate the volume expansion and avoid the structural collapse[2, 14, 15].

In addition to PIBs with promising prospect. So far, many kinds of rechargeable Zn-ion energy storage devices, such as Zn-ion capacitors, Zn-ion batteries and Zn-air batteries, have been widely studied owing to their high safety based on the aqueous electrolyte[16-18]. Among them, aqueous Zn-ion hybrid supercapacitor (ZHS) is a newly-emerged energy storage device, which is usually composed of zinc metal anode and carbon-based cathode. ZHS is considered as one of the most attractive energy storage devices by combining the merits of batteries and supercapacitors[19-22]. For instance, Zhang et al.[21] studied the use of hierarchically porous carbon as cathode in ZHS, which displayed a high energy density of 107.3 Wh kg^{-1} and a superb power density of 24.9 kW kg^{-1}.

Herein, calcium gluconate was firstly introduced as a carbon source for constructing ultrathin hierarchically porous carbon nanosheets with a facile *in situ* template method. The specific surface

area and porosity of carbon materials can be precisely tuned by adjusting the calcination temperatures. The as-obtained Ca-900 electrode exhibits superior K-ion storage performance including high reversible capacity (430.7 mAh g^{-1}), high rate capability (5.0 A g^{-1}) and ultra-long cycling stability (4000 cycles at 1.0 A g^{-1}). The superiority and universality of the Ca-900 electrode is further verified in zinc-ion hybrid supercapacitor, which delivers high energy density (134.5 Wh kg^{-1}) and power density (9.3 kW kg^{-1}) as well as a high capacitance retention (~90.9%) over 4000 cycles. Moreover, to excavate the origin of the excellent electrochemical performance, a carefully designed consecutive CV measurement was introduced. The predominant capacitive behaviors, rooting in the high specific surface area and highly developed porous structure, are confirmed the main contribution of the unprecedent electrochemical performance. Overall, this work may open a new window for understanding the metal-ion storage behaviors with carbonaceous electrode materials.

2. Experimental Section

2.1 Preparation of Ca-x materials: Ultrathin porous carbon nanosheets are prepared by using calcium gluconate ($Ca(C_6H_{11}O_7)_2$) as the carbon source followed by a carbonization treatment and an acid etching process. Specifically, a certain amount of calcium gluconate powder (5.0 g) is weighed and placed evenly in a quartz boat, which is subsequently transferred to the tube furnace and pyrolyzed at selected temperatures (600, 700, 800, 900 and 1000 ℃, holding for 1h) with a temperature ramp rate of 5 ℃ min^{-1} under Ar flow protection (100 mL min^{-1}). After natural cooling, the precursors can be obtained (denoted as Ca-x-P, x stands for the carbonization temperature). Afterwards, the precursors are washed for three times with diluted hydrochloric acid (~1.2 mol/L), deionized water and anhydrous ethanol, respectively. After a vacuum drying process at 70 ℃ for 10 h followed by a soft grinding process in the mortar, the ultrathin porous carbon materials are collected and denoted as Ca-x.

2.2 Structural characterization: X-Ray Diffraction (XRD) analysis was performed on a Rigaku Miniflex 600 X-ray diffractometer with Cu Kα radiation (λ=1.5406Å) at a scan rate of 5°/min. Morphological and microstructural characterizations were conducted on Scanning electronic microscope (SEM, Phenom Pro and JEOL JSM-7610F) and Transmission electronic microscope (TEM, JEOL JEM-2100). The specific surface area and pore structure information were collected by N_2 adsorption isotherm at -196 ℃ on a Micromeritics ASAP 2020 analyzer. The samples were dried and degassed at 200 ℃ for 8 hours before testing. Raman spectra were collected on a Rennishaw inVia confocal Raman spectrometer using a 633 nm laser as the excitation source.

2.3 Electrochemical measurement

Potassium-ion batteries: Electrode materials are prepared by mixing 80 wt% active material (as-prepared Ca-x), 10 wt% super P and 10 wt% polyvinylidene fluoride (PVDF) in the NMP (N-methyl-2-pyrrolidone) solvent under magnetic stirring to form a uniform slurry. Afterward, the slurry is coated onto a copper foil followed by a vacuum drying process (100 ℃ for 10 h) to evaporate the solvent. After natural cooling, the dried foil is cut into circular electrodes with a diameter of 12 mm. K-ion cell is assembled in an argon-filled glovebox using CR2032-type coin cells with K-metal foil as the counter electrode. A whatman GF/D glass fiber filter is applied as the separator. The electrolyte is 0.8 M KPF_6 dissolved in ethylene carbonate and diethyl carbonate (EC/DEC=1:1 by volume). The electrochemical measurements are evaluated within a voltage range of 0.01~3.0 V using a LAND-CT2001A multichannel galvanostat (Wuhan, China) at 25°C. Cyclic voltammetry (CV) is acquired on a CHI 660E electrochemical workstation.

Zinc-ion capacitors: The electrode is prepared by mixing active material, conductive material carbon (super P) and polytetrafluoroethylene (PTFE) in the mass proportion of 85:10:5 with NMP as solvent followed by magnetic stirring to form a homogeneous slurry. The slurry is evenly smeared on the cleaned carbon paper followed by a vacuum drying process at 100 ℃ for 10 h. After natural

cooling, the dried carbon paper is cut into circular electrodes with a diameter of 12 mm. Zinc foil is applied as the counter electrode, commercial filter paper is used as the separator, and the electrolyte is 1.0 M zinc sulfate ($ZnSO_4$) dissolved in deionized water. All capacitors are assembled with CR2032-type coin cells. The electrochemical performance is evaluated on LAND-CT2001A multichannel galvanostat within the voltage range of 0~1.8 V, and the CV test results are obtained by a CHI660E electrochemical workstation.

3.Results and discussion

3.1 Morphological and microstructural analyses

The synthetic process of the ultra-thin carbon nanosheets is illustrated in **Fig. 1**. Calcium gluconate was introduced as the carbon source. By controlling the calcination temperatures, various kinds of Ca-based hard template can be *in situ* generated. Followed by an acid etching process, the template can be easily removed and porous carbon nanosheets can be obtained. TEM observations were conducted to reveal the morphological evolutions. As shown in **Fig. 1 and Fig. S1**, after the calcination treatment, evenly distributed nanoparticles can be clearly distinguished on the ultrathin carbon nanosheets, which vanish after the acid etching process and ultrathin carbon nanosheets with uniformly distributed nanosized pores can be obtained.

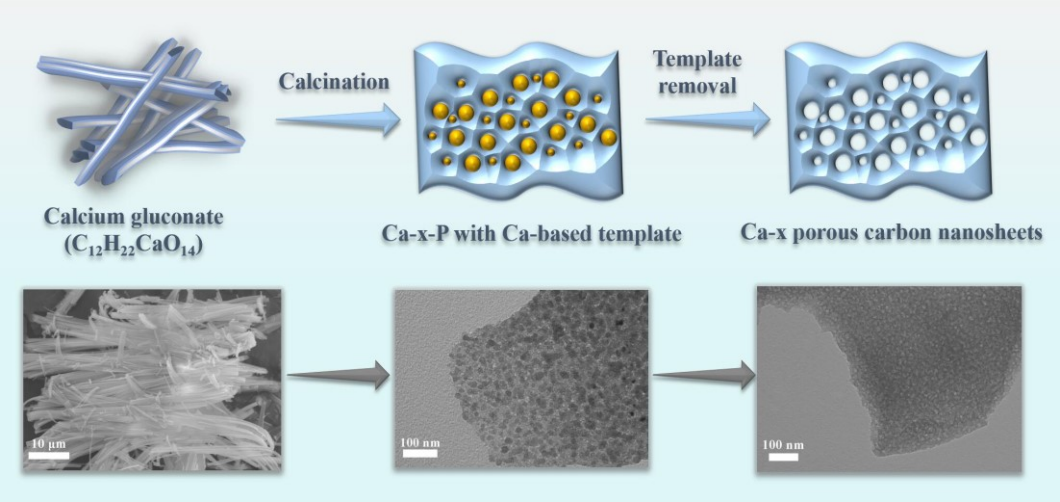

Fig.1 Schematic illustrations of the synthetic process. (a) SEM images of calcium gluconate. (b) TEM image of Ca-900-P and (c) Ca-900.

The TEM images of Ca-x exhibit a translucent characteristic (**Fig. 1c** and **S1**), indicating an ultrathin feature. The SEM images further verify this morphology (**Fig. 2a-b** and **S2**), the obtained Ca-x at various temperatures all exhibit an ultrathin thickness in the range of 20~30 nm (**Fig. 2c**), which will significantly shorten the diffusion lengths of tested metal ions and indicate a fast transport kinetics. XRD was further employed to track the phase transformations. As depicted in **Fig. 2d**, the *in situ* generated template can be determined as $CaCO_3$ (PDF#47-1743) under pyrolyzed temperatures below 800℃, which further decomposes into CaO (PDF#48-1467) and CO_2 at higher temperatures. The detected $Ca(OH)_2$ (PDF#44-1481) signals at high temperatures (800-1000℃) should be ascribed to the moisture sensitive feature of CaO. Except the template virtue of the Ca-based nanoparticles, the released CO_2 gas can also play a vital role in creating micropores by etching the carbon matrix, which will be verified and discussed in **Fig. 3**. The involved reactions are summarized as follows:

$$CaCO_3 \rightarrow CaO + CO_2 \quad (1)$$

$$CO_2 + C \rightarrow CO \quad (2)$$

The EDS result is displayed in **Fig. S3**, the increasing C/O ratio (Ca-600 is 6.11 and Ca-900 is 9.91) at higher temperature indicates the decomposition of oxygen-containing groups, which will benefit the electronic conductivity. At this point, Ca-x obtained at relatively high temperature will exhibit better battery performance. XRD patterns after the acid etching process were displayed in **Fig. 2e**. The obtained Ca-x all exhibit a broad peak at ~22.8° and a weak peak at ~44°, corresponding to the (002) and (101) crystal indexes of graphite. The broad peak indicates a relatively amorphous structure of the porous carbon nanosheets. Besides, the lower angel shifted (002) peak compared with the standard pattern (PDF#75-1621) means an enlarged interlayer spacing, which can be determined by the Bragg equation[23]:

$$2dsin\theta = \lambda \quad (3)$$

And the interlayer spacing can be obtained by the deformation:

$$d = \frac{\lambda}{2sin\theta} \quad (4)$$

Herein, λ is the wave length of the Cu Kα radiation (=1.5406 Å). Therefore, the interlayer spacing of the obtained Ca-x is calculated to be ~0.39 nm, higher than graphite (~0.34 nm). The expanded lamellar spacing is conducive to the rapid diffusion of metal ions, especially for K ions with larger ionic radius. Hence an enhanced rate capability can be expected.

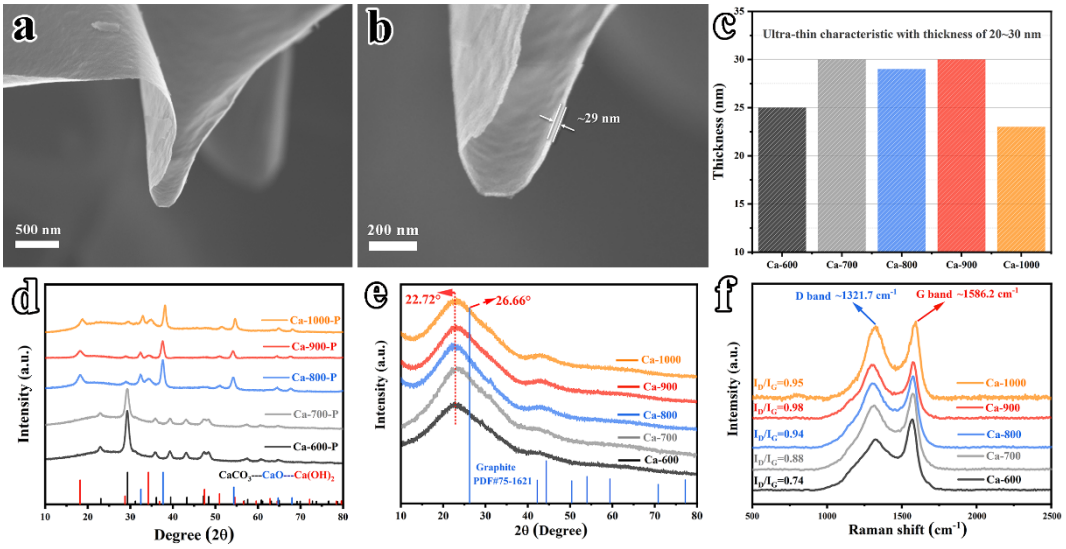

Fig.2 Morphological and structural characterizations. (a-b) SEM images of Ca-900. (c) A survey of the thickness of Ca-x. XRD patterns of (d) precursors Ca-x-P and (e) obtained carbon nanosheets Ca-x. (f) Raman spectra of Ca-x.

Moreover, Raman spectra were collected to grasp a better understanding of the carbon structure. As shown in **Fig. 2f**, two obvious peaks near 1322 cm^{-1} and 1586 cm^{-1} can be observed, corresponding to the characteristic D band and G band of graphite. D band represents the defect or disorder degree, while G band reflects the in-plane stretching vibration of the sp^2 hybrid structure. Therefore, the I_D/I_G ratio can interpret the degree of graphitization or disorder. Specifically, the

calculated ratios increase with higher carbonization temperature (from 0.74 of Ca-600 to 0.95 of Ca-1000), indicating a more disorder/defective structure, which will provide sufficient accessible sites and diffusion pathways for the fast diffusion of metal ions.

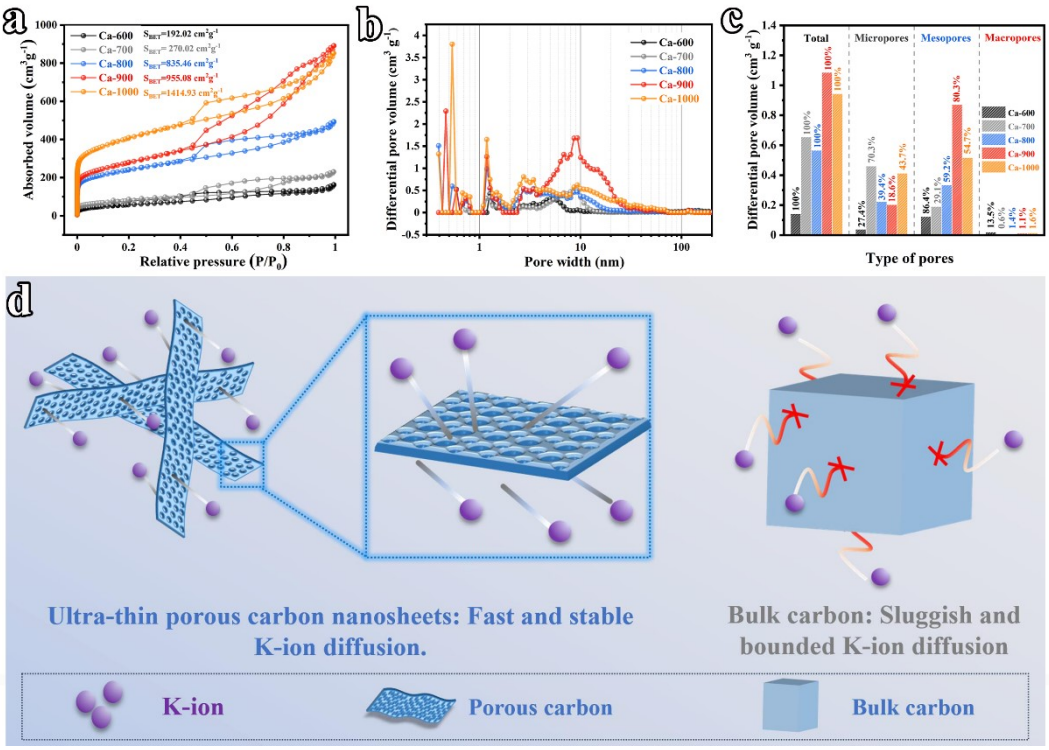

Fig.3 Pore structure evaluations. (a) Nitrogen adsorption–desorption isotherms. (b) Pore size distributions. (c) Pore volume contribution ratios of micropores, mesopores and macropores. (d) Schematic diagram of K-ion diffusion kinetics in the hierarchically porous ultrathin carbon nanosheets.

In the case of carbonaceous materials, a high disorder degree is always associated with a well developed porous structure[24]. As plotted in **Fig 3a**. the N_2 adsorption-desportion curves of Ca-x all exhibit a combination of type I (uptake at the low P/P_0 region, characteristic of micropores) and type IV (hysterisis loop at the low P/P_0 region, characteristic of mesopores) isotherms. Besides, the uplift of the curve at high P/P_0 region corresponds to the existencce of macropores and this morphology has been clearly distinguished by SEM and TEM results (**Fig. 1**, **Fig. S1** and **Fig. 2a-b**). Therefore, all of the Ca-x samples exhibit hierarchically porous structures with high specific surface areas (192.02, 270.02, 835.46, 955.08 and 1414.93 $m^2 g^{-1}$ for Ca-600, Ca-700, Ca-800, Ca-900 and Ca-1000, respectively). Among them, the hysteresis loop area of Ca-900 is the largest, which indicates abundant existence of mesopores. This structure provides sufficient channels and spaces for the diffusion of metal ions and alleviation of the volume expansion, which further contributes to enhanced rate performance and cycling stability [25, 26].

The unique porous structure is further dissected by the results of pore size distributions. As plotted in **Fig. 3b**, the hierarchically porous structure is solidified with peaks centered at the whole region of 0.4~100 nm. Specifically, Ca-900 shows the strongest peak centered at ~10 nm, which is in accordance with the results of **Fig. 3a**. Besides, Ca-x samples obtained at high temperatures (≧

800°C) exhibit stronger peaks centered at micropore and mesopore region, which should originate from the decomposition process of $CaCO_3$ at high temperatures. The *in situ* generated CO_2 gas is a very effective pore-forming agent (similar as KOH) by etching the carbon matrix (see **formula 2**), which is conducive to create pores, especially micropores. Moreover, the higher the temperature, the higher the pore-making activity of CO_2, which is consistent with the results of Raman spectra. Abundant micropores serve as defective sites and express a higher I_D/I_G value. Furthermore, the pore volume of Ca-x is concluded in **Fig. 3c**, consistently, Ca-900 exhibits the highest pore volume (1.08 cm^3 g^{-1}) and highest proportion of mesopores (80.3%), indentifying its highly developed porous structure.

Briefly speaking, the facilely prepared Ca-x samples with ultrathin hierarchically porous structure exhibit great potentials for large-sized K-ion storage (**Fig. 3d**), the reasons can be concluded as follows: **i)** High specific surface areas (SSA) can guarantee sufficient contact between the electrolyte and electrode surface; **ii)** Highly developed porous structure can provide sufficient and broad K-ion diffusion channels, thus enabling fast and stable K-ion diffusion. **iii)** Abundant micropores alongwith high SSA can serve as extra sites for capacitive K-ion adsorption, improving the reversible specifica capacities. **iV)** Ultrathin characteristic shortens the diffusion lengths and ensures fast K-ion transport kinetics.

3.2 Electrochemical performance

The cycling performance of Ca-x based PIBs was firstly evaluated (**Fig. 4a**). After being cycled at 100 mA g^{-1} for 100 cycles, Ca-900 electrode delivers the highest capacity of 235.4 mAh g^{-1}, while the rest electrodes can only maintain capacities lower than 200 mAh g^{-1}. Simultaneously, it can be observed that the coulombic efficiencies of all samples in the initial cycles are relatively low and gradually increase to 100% in the following cycles. This phenomenon can be attributed to the large SSA which consumes more electrolyte to form a stable SEI (solid electrolyte interface) layer on the electrode surface. In view of the unique ultrathin and porous structure of Ca-x, the rate capability was then investigated. As depicted in **Fig. 4b**, Ca-900 electrode delivers higher capacities than the rest electrodes at all current densities. The specific values of reversible capacities at each current density are concluded in **Fig. 4c**. Particularly, Ca-900 electrode can release a high capacity of 430.7 mAh g^{-1}, while the rest electrodes can only deliver capacities below 400 mAh g^{-1}. Besides, Ca-900 electrode can suffer fast potassiation/de-potassiation shock and maintain a relatively high capacity of 154.8 mAh g^{-1} at ultrahigh current density of 5.0 A g^{-1}, corresponding to the highest capacity retention ratio of 35.8% among all the Ca-x electrodes. When the current density is set back to 0.05 mA g^{-1}, the reversible capacity of Ca-900 electrode can also recover to 383.7 mAh g^{-1} (89.1% retention), further verifying the superior electrode stability of Ca-900 at high current densities, while the rest electrodes suffer sever structural deformation and gradually lose the electrochemical activity.

Intrigued by the excellent rate capability of Ca-900 electrode, the long-term cycling stability

was evaluated at high current density of 1.0 A g^{-1}. As shown in **Fig. 4d**, Ca-900 electrode delivers a capacity retention ratio of 81.2% after 4000 cycles, corresponding to a capacity loss ratio of 0.0047% per cycle, outmatching most of the reported carbon electrodes[27].

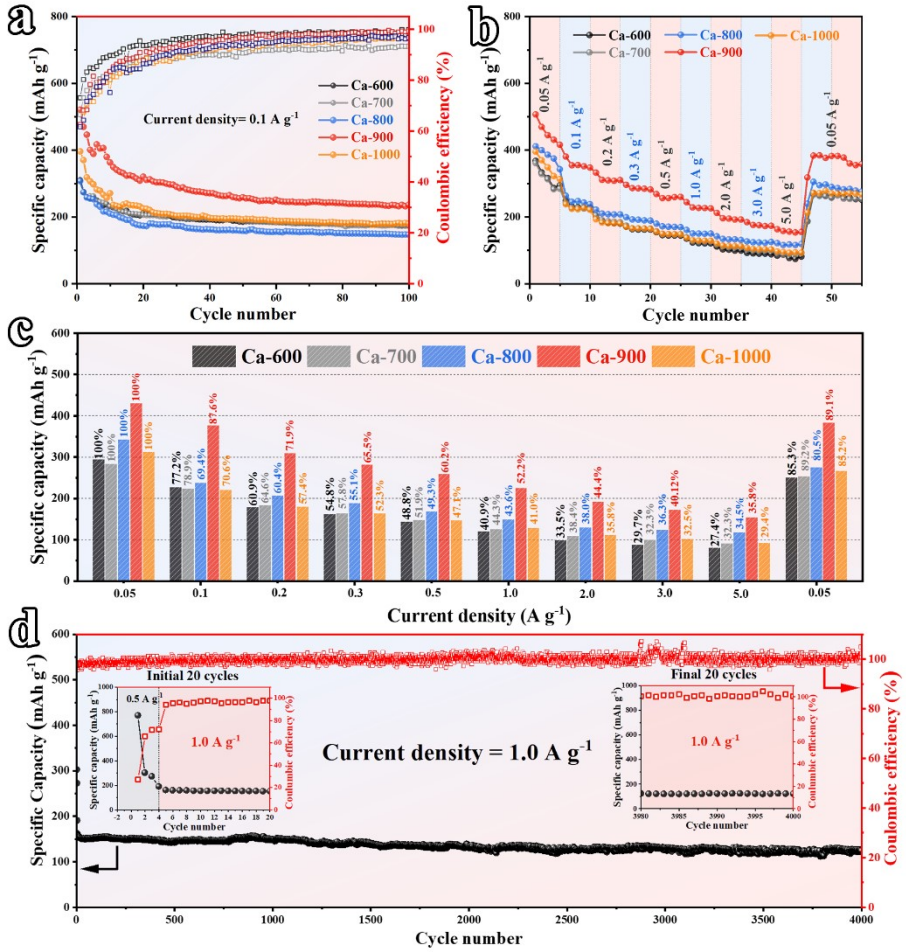

Fig.4 Electrochemical performance of Ca-x electrodes in PIBs. (a) Cycling performance. (b) Rate capability at various current densities. (c) Capacity retention ratios at various current densities. (d) Long-term cycling stability at 1.0 A g^{-1} (the electrode was preactivated at 0.05A g^{-1} for 3 cycles).

To track the origin of the superior rate capability, consecutive CV measurements were conducted at various scan rates of 0.1 to 1.0 mV s^{-1} (**Fig. 5a** and **Fig. S4**). The corresponding relationship between peak current and scan rate can be obtained by these curves: $\boldsymbol{i = av^b}$, where $\boldsymbol{a}$ and $\boldsymbol{b}$ are adjustable constants. The $\boldsymbol{b}$ value can be obtained from the slope by plotting **log (*i*) *vs.* log (*v*)**[28, 29]. Specifically, when $\boldsymbol{b}$ value is approaching 0.5, the tested electrode is dominated by the battery behavior (relatively sluggish), corresponding to the diffusion process. When $\boldsymbol{b}$ value is close to 1.0, capacitive behavior predominates alongwith the adsorption process (kinetic favorable)[30]. The calculated $\boldsymbol{b}$ values are concluded in **Fig. 5b** and **Fig. S4**, it can be observed that $\boldsymbol{b}$ value varies at different potassiation depths. To parse this phenomenon, the calculated $\boldsymbol{b}$ values at various potentials are concluded in **Fig. 5c**, and we come to a preliminary conjecture that capacitive K-ion storage process mainly takes place within the potential range of 0.4~2.0 V (vs. K/K^+) with higher $\boldsymbol{b}$ values. Moreover, the mixed behaviors were quantified by the following equations: $\boldsymbol{i = k_1 v + k_2 \sqrt{v}}$.

Herein, k_1 and k_2 are constants, $k_1 v$ stands for the capacitive contribution, while $k_2\sqrt{v}$ represents the contribution of diffusion-controlled behavior. As plotted in **Fig. 5d** and **Fig. S4**, the red part represents the capacitive contribution, which dominates the total capacity (66.02% for Ca-900, higher than the rest electrodes). Specially, the red part occupies a higher ratio in the region higher than 0.4 V, consistent with the variation tendency of ***b*** values. Moreover, the capacitive contribution ratios of all Ca-x samples are concluded in **Fig. 5e**, Ca-900 electrode is the highest at all scan rates, which is also consistent with its best electrochemical performance.

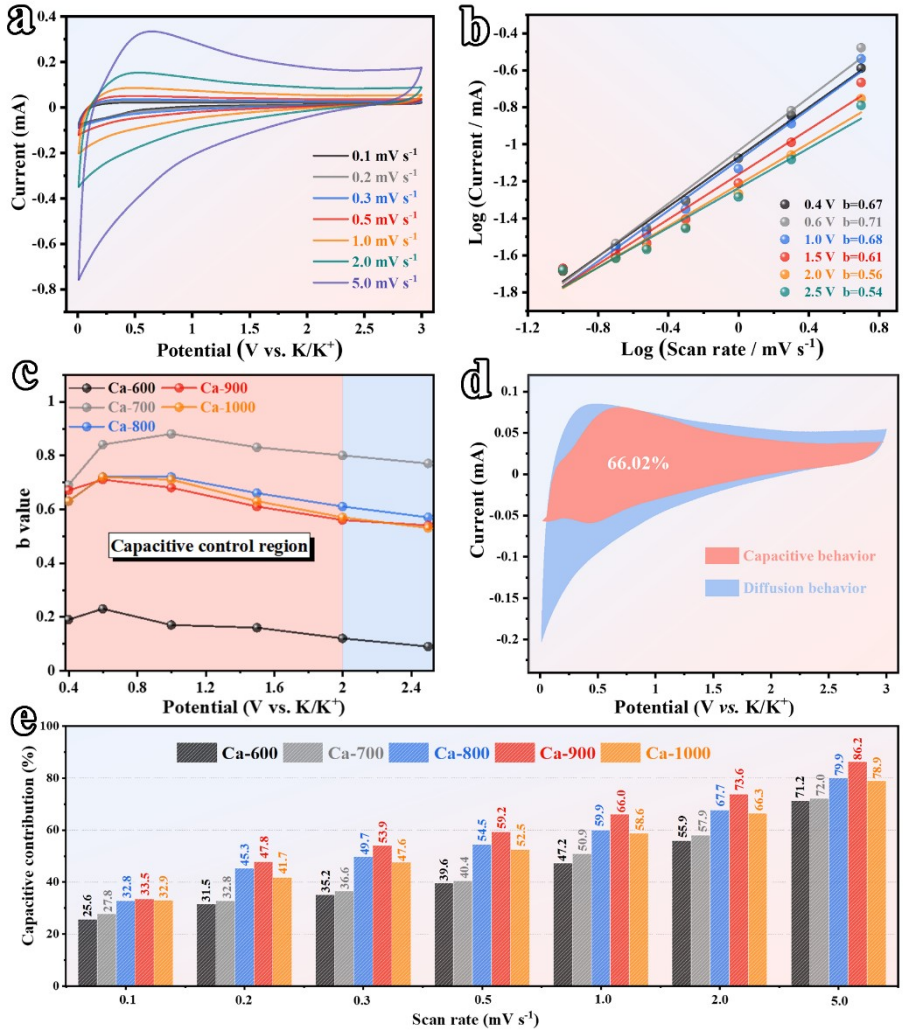

Fig.5 Kinetic evaluations of Ca-x electrodes in PIBs. (a) CV curves of Ca-900 electrode at various scan rates. (b) ***b*** values of Ca-900 electrode determined at various potassiation depths. (c) ***b*** values of all Ca-x electrodes. (d) Sketch of the capacitive contribution at 1.0 mV s^{-1}. (e) Capacitive contribution ratios of Ca-x electrodes at various scan rates.

Zinc-ion hybrid supercapacitors (ZHSs) have received extensive attentions owing to the rich zinc sources, low cost, and high safety[22, 31]. The negative electrode material for ZHSs is usually a carbon-based material with a high specific surface area[32, 33]. Therefore, our carefully designed Ca-900 with unique ultrathin hierarchically porous structure shows great potential in ZHSs.

CV measurements were firstly conducted at different scan rates (5.0 mV s^{-1}~200 mV s^{-1}) to investigate the Zn-ion storage behavior. As shown in **Fig. 6a**, weak redox peaks can be observed,

representing the pseudo-capacitive behavior. Similarly, the ***b*** values can be extracted from the CV curves at various potentials (**Fig. 6b**), which are undoubtedly higher than that of PIBs, indicating the capacitive inherence of ZHSs[34]. The contribution of capacitive behavior was plotted in **Fig. 6c**, unlike the plot of PIBs, the red part distributed evenly within the tested potential range, further confirming the capacitive nature of ZHSs. Besides, Ca-900 electrode delivers high capacitive contribution ratios at all scan rates, especially at a superhigh scan rate of 200 mV s^{-1} (**Fig. 6d**). Consequently, Ca-900 electrode exhibits a good rate capability with a high capacity retention ratio of ~40% at 2.0 A g^{-1}. (**Fig. 6e** and **Fig. S5**). Besides, when current density returns to 0.1 A g^{-1}, the capacity is just slightly lower than the initial cycles, indicating a high reversibility. To study the practical prospect, the energy density and power density were calculated and concluded as Ragone plot in **Fig. 6f**. When power density is 1.8 kW kg^{-1}, a high energy density of 134.5 Wh kg^{-1} is achieved. When power density increases to 9.3 kW kg^{-1}, the power density is still as high as 98.6 Wh kg^{-1}. Compared with reported carbon-based ZHSs, such as HNPC//Zn[35], AC//AC[36], Graphene//Graphene[37], MPCs//Zn[38], $RuO_2 \cdot H_2O$//Zn[22], MDC//Zn[39], a-MEGO//Zn[40], HPC//Zn[41] and HSC//Zn[19], our Ca-900 electrode shows the best overall electrochemical performance. Moreover, Ca-900 electrode also exhibits superior cycling stability at a high current density of 1.0 A g^{-1} with a neglectable capacity loss ratio of 0.0023% per cycle, further solidifying the effectiveness of the ultrathin porous structure in capacitive energy storage systems (**Fig. 6g**).

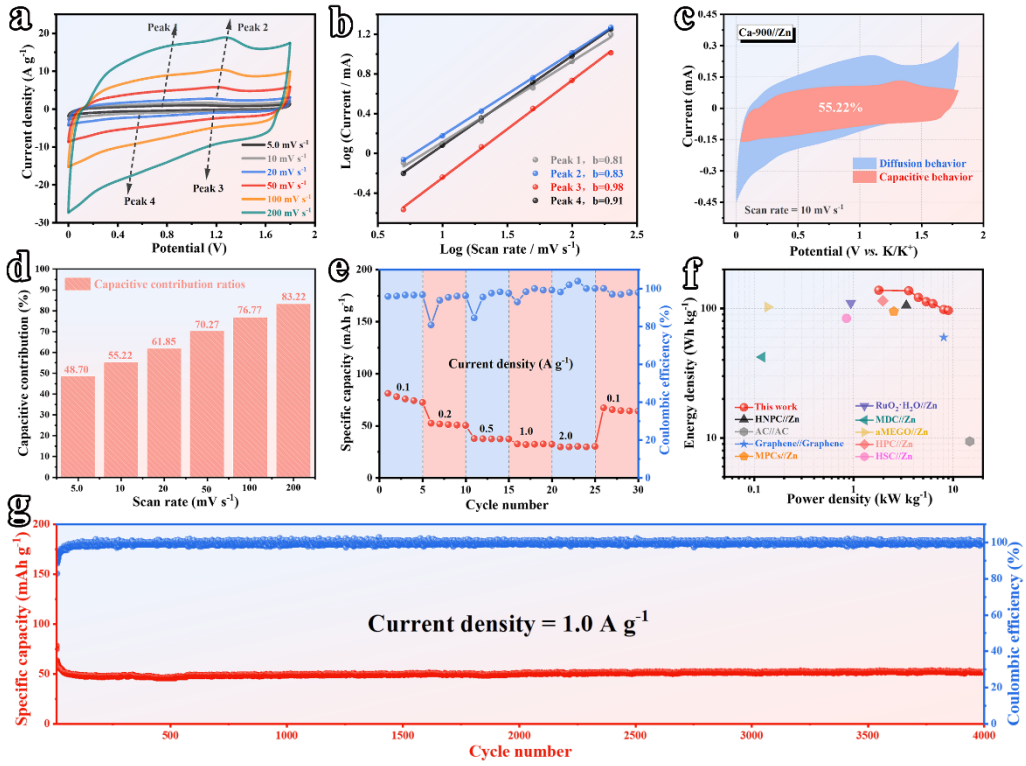

Fig.6 Electrochemical performance of Ca-900//Zn in Zn-ion capacitors. (a) CV curves at various scan rates. (b) ***b*** values at various scan rates. (c) Sketch of capacitive contribution at 10 mV s^{-1}. (d) Capacitive contribution ratios at various scan rates. (e) Rate performance at various current densities. (f) Ragone plots. (g) Long-term cycling

performance.

4. Conclusion

In summary, we propose a facile preparation strategy for constructing ultrathin porous carbon materials by direct pyrolyzing calcium gluconate. The obtained carbons show ultrathin characteristic (thickness of 20~30 nm) and hierarchically porous structure (high SSA of 955.08 $m^2 g^{-1}$ and pore volume of 1.08 $cm^3 g^{-1}$). Therefore, the as-prepared Ca-900 electrode delivers excellent electrochemical performance in PIBs with high reversible capacity (430.7 mAh g^{-1}), excellent rate capability (158.4 mAh g^{-1} at 5.0 A g^{-1}) and ultra-stable cycling performance (over 4000 cycles at 1.0 A g^{-1}). In virtue of the carefully designed consecutive CV measurements, it is confirmed that the unique porous structure contributes to predominant capacitive metal-ion storage, thus resulting in the significantly improved battery performance. Moreover, we dissect the mixed behaviors at various potassiation depths and we draw a conclusion that capacitive behavior dominates in the range of 0.4~2.0 V with carbon-based anode materials. Furthermore, Ca-900 electrode also exhibits remarkable Zn-ion storage capability with a capacity retention ratio of ~90.9% after 4000 cycles at 1.0 A g^{-1}. Considering the facile preparation strategy, unique microstructure, outstanding electrochemical performance and in-depth mechanism investigations, we believe this work will strength the fundamental understandings of porous carbons and boost the development of carbon-based energy storage devices like K-ion/Na-ion/Li-ion batteries/capacitors, Al-ion batteries, Zn-ion capacitors and Dual-ion capacitors, etc.

Acknowledgment

This work was supported by High-level Talents' Discipline Construction Fund of Shandong University (Grant No. 31370089963078), School Research Startup Expenses of Harbin Institute of Technology (Shenzhen) (Grant No. DD29100027), China Postdoctoral Science Foundation (Grant No. 2019M661276), Guangdong Basic and Applied Basic Research Foundation (Grant No. 2019A1515110756).

References

1. Dunn, B.; Kamath, H.; Tarascon, J.-M., Electrical Energy Storage for the Grid: A Battery of Choices. *Science* **2011,** *334* (6058), 928.

2. Li, D.; Ren, X.; Ai, Q.; Sun, Q.; Zhu, L.; Liu, Y.; Liang, Z.; Peng, R.; Si, P.; Lou, J.; Feng, J.; Ci, L., Facile Fabrication of Nitrogen-Doped Porous Carbon as Superior Anode Material for Potassium-Ion Batteries. *Advanced Energy Materials* **2018,** *8* (34), 1802386.

3. Xu, Y.; Zhang, C.; Zhou, M.; Fu, Q.; Zhao, C.; Wu, M.; Lei, Y., Highly nitrogen doped carbon nanofibers with superior rate capability and cyclability for potassium ion batteries. *Nature communications* **2018,** *9* (1), 1720.

4. Jian, Z.; Xing, Z.; Bommier, C.; Li, Z.; Ji, X., Hard carbon microspheres: potassium-ion anode versus sodium-ion anode. *Advanced Energy Materials* **2016,** *6* (3), 1501874.

5. Xu, Y.; Zhou, M.; Wang, X.; Wang, C.; Liang, L.; Grote, F.; Wu, M.; Mi, Y.; Lei, Y., Enhancement of Sodium Ion Battery Performance Enabled by Oxygen Vacancies. *Angewandte Chemie International Edition* **2015,** *54* (30), 8768-8771.

6. Wang, G.; Xiong, X.; Xie, D.; Lin, Z.; Zheng, J.; Zheng, F.; Li, Y.; Liu, Y.; Yang, C.; Liu, M., Chemically activated hollow carbon nanospheres as a high-performance anode material for potassium ion batteries. *Journal of Materials Chemistry A* **2018,** *6* (47), 24317-24323.

7. Li, D.; Zhang, Y.; Sun, Q.; Zhang, S.; Wang, Z.; Liang, Z.; Si, P.; Ci, L., Hierarchically porous carbon supported Sn_4P_3 as a superior anode material for potassium-ion batteries. *Energy Storage Materials* **2019,** *23*, 367-374.

8. Wu, Y.; Huang, H.-B.; Feng, Y.; Wu, Z.-S.; Yu, Y., The Promise and Challenge of Phosphorus-Based Composites as Anode Materials for Potassium-Ion Batteries. *Advanced Materials* **2019,** *31* (50), 1901414.

9. Zhang, W.; Mao, J.; Li, S.; Chen, Z.; Guo, Z., Phosphorus-Based Alloy Materials for Advanced Potassium-Ion Battery Anode. *Journal of the American Chemical Society* **2017,** *139* (9), 3316-3319.

10. Tan, H.; Feng, Y.; Rui, X.; Yu, Y.; Huang, S., Metal Chalcogenides: Paving the Way for High-Performance Sodium/Potassium-Ion Batteries. *Small Methods* **2020,** *4* (1), 1900563.

11. Wang, Z.; Selbach, S. M.; Grande, T., Van der Waals density functional study of the energetics of alkali metal intercalation in graphite. *Rsc Advances* **2014,** *4* (8), 4069-4079.

12. Zhang, W.; Liu, Y.; Guo, Z., Approaching high-performance potassium-ion batteries via advanced design strategies and engineering. *Science advances* **2019,** *5* (5), eaav7412.

13. Wang, L.; Guo, C.; Zhu, Y.; Zhou, J.; Fan, L.; Qian, Y., A $FeCl_2$-graphite sandwich composite with Cl doping in graphite layers: a new anode material for high-performance Li-ion batteries. *Nanoscale* **2014,** *6* (23), 14174-14179.

14. Wang, F.; Yi, J.; Wang, Y.; Wang, C.; Wang, J.; Xia, Y., Graphite Intercalation Compounds (GICs): A New Type of Promising Anode Material for Lithium-Ion Batteries. *Advanced Energy Materials* **2014,** *4* (2), 1300600.

15. Wang, L.; Zhu, Y.; Guo, C.; Zhu, X.; Liang, J.; Qian, Y., Ferric chloride-Graphite Intercalation Compounds as Anode Materials for Li-ion Batteries. *ChemSusChem* **2014,** *7* (1), 87-91.

16. Zhang, X.; Pei, Z.; Wang, C.; Yuan, Z.; Wei, L.; Pan, Y.; Mahmood, A.; Shao, Q.; Chen, Y., Flexible Zinc-Ion Hybrid Fiber Capacitors with Ultrahigh Energy Density and Long Cycling Life for Wearable Electronics. *Small* **2019,** *15* (47), 1903817.

17. Xu, C.; Li, B.; Du, H.; Kang, F., Energetic Zinc Ion Chemistry: The Rechargeable Zinc Ion Battery. *Angewandte Chemie* **2012,** *51* (4), 933-935.

18. Olsson, E.; Hussain, T.; Karton, A.; Cai, Q., The adsorption and migration behavior of divalent metals (Mg, Ca, and Zn) on pristine and defective graphene. *Carbon* **2020**, 163, 276-287.

19. Wang, H.; Wang, M.; Tang, Y., A novel zinc-ion hybrid supercapacitor for long-life and low-cost energy storage applications. *Energy Storage Materials* **2018,** *13*, 1-7.

20. Dong, L.; Ma, X.; Li, Y.; Zhao, L.; Liu, W.; Cheng, J.; Xu, C.; Li, B.; Yang, Q.; Kang, F., Extremely safe, high-rate and ultralong-life zinc-ion hybrid supercapacitors. *Energy Storage Materials* **2018,** *13*, 96-102.

21. Zhang, H.; Liu, Q.; Fang, Y.; Teng, C.; Liu, X.; Fang, P.; Tong, Y.; Lu, X., Boosting Zn-Ion Energy Storage Capability of Hierarchically Porous Carbon by Promoting Chemical Adsorption. *Advanced Materials* **2019,** *31* (44), 1904948.

22. Dong, L.; Yang, W.; Yang, W.; Wang, C.; Li, Y.; Xu, C.; Wan, S.; He, F.; Kang, F.; Wang, G., High-Power and Ultralong-Life Aqueous Zinc-Ion Hybrid Capacitors Based on Pseudocapacitive Charge Storage. *Nano-micro Letters* **2019,** *11* (1), 94.

23. Pope, C. G., X-Ray Diffraction and the Bragg Equation. *Journal of Chemical Education* **1997,** *74* (1), 129-131.

24. Li, D.; Chen, L.; Chen, L.; Sun, Q.; Zhu, M.; Zhang, Y.; Liu, Y.; Liang, Z.; Si, P.; Lou, J., Potassium gluconate-derived N/S Co-doped carbon nanosheets as superior electrode materials for supercapacitors and sodium-ion batteries. *Journal of Power Sources* **2019,** *414*, 308-316.

25. Li, D.; Sun, Q.; Zhang, Y.; Chen, L.; Wang, Z.; Liang, Z.; Si, P.; Ci, L., Surface-Confined SnS_2@C@rGO as

High-Performance Anode Materials for Sodium- and Potassium-Ion Batteries. *ChemSusChem* **2019,** *12* (12), 2689-2700.

26. Xiao, M.; Zhu, J.; Feng, L.; Liu, C.; Xing, W., Meso/Macroporous Nitrogen-Doped Carbon Architectures with Iron Carbide Encapsulated in Graphitic Layers as an Efficient and Robust Catalyst for the Oxygen Reduction Reaction in Both Acidic and Alkaline Solutions. *Advanced Materials* **2015,** *27* (15), 2521-2527.

27. Wu, X.; Chen, Y.; Xing, Z.; Lam, C. W. K.; Pang, S.-S.; Zhang, W.; Ju, Z., Advanced Carbon-Based Anodes for Potassium-Ion Batteries. **2019,** *9* (21), 1900343.

28. Cui, Y.; Liu, W.; Wang, X.; Li, J.; Zhang, Y.; Du, Y.; Liu, S.; Wang, H.; Feng, W.; Chen, M., Bioinspired Mineralization under Freezing Conditions: An Approach to Fabricate Porous Carbons with Complicated Architecture and Superior K^+ Storage Performance. *ACS Nano* **2019,** *13* (10), 11582-11592.

29. Liu, L.; Lin, Z.; Chane-Ching, J.-Y.; Shao, H.; Taberna, P.-L.; Simon, P., 3D rGO aerogel with superior electrochemical performance for K–Ion battery. *Energy Storage Materials* **2019,** *19*, 306-313.

30. Zhang, Y.; Chen, L.; Hao, C.; Zheng, X.; Guo, Y.; Chen, L.; Lai, K.; Zhang, Y.; Ci, L., Potassium pre-inserted $K_{1.04}Mn_8O_{16}$ as cathode materials for aqueous Li-ion and Na-ion hybrid capacitors. *Journal of Energy Chemistry* **2020,** *46*, 53-61.

31. Wei, T.; Li, Q.; Yang, G.; Wang, C., Pseudo-Zn–Air and Zn-Ion Intercalation Dual Mechanisms to Realize High-Areal Capacitance and Long-Life Energy Storage in Aqueous Zn Battery. *Advanced Energy Materials* **2019,** *9* (34), 1901480.

32. Zheng, Y.; Zhao, W.; Jia, D.; Liu, Y.; Cui, L.; Wei, D.; Zheng, R.; Liu, J., Porous carbon prepared via combustion and acid treatment as flexible zinc-ion capacitor electrode material. *Chemical Engineering Journal* **2020,** *387*, 124161.

33. Liu, P.; Gao, Y.; Tan, Y.; Liu, W.; Huang, Y.; Yan, J.; Liu, K., Rational design of nitrogen doped hierarchical porous carbon for optimized zinc-ion hybrid supercapacitors. *Nano Research* **2019,** *12* (11), 2835-2841.

34. Chen, Y.; Qin, L.; Lei, Y.; Li, X.; Dong, J.; Zhai, D.; Li, B.; Kang, F., Correlation between Microstructure and Potassium Storage Behavior in Reduced Graphene Oxide Materials. *ACS Applied Materials & Interfaces* **2019,** *11* (49), 45578-45585.

35. Zhang, H.; Liu, Q.; Fang, Y.; Teng, C.; Liu, X.; Fang, P.; Tong, Y.; Lu, X., Boosting Zn-Ion Energy Storage Capability of Hierarchically Porous Carbon by Promoting Chemical Adsorption. *Advanced Materials* **2019**, 31(44), 1904948.

36. Liu, J.; Guan, C.; Zhou, C.; Fan, Z.; Ke, Q.; Zhang, G.; Liu, C.; Wang, J., A flexible quasi-solid-state nickel–zinc battery with high energy and power densities based on 3D electrode design. *Advanced materials* **2016,** *28* (39), 8732-8739.

37. Dong, S.; Xu, Y.; Wu, L.; Dou, H.; Zhang, X., Surface-functionalized graphene-based quasi-solid-state Na-ion hybrid capacitors with excellent performance. *Energy Storage Materials* **2018,** *11*, 8-15.

38. Jiang, C.; Zou, Z., Waste polyurethane foam filler-derived mesoporous carbons as superior electrode materials for EDLCs and Zn-ion capacitors. *Diamond and Related Materials* **2019**, 101, 107603.

39. Xiong, T.; Shen, Y.; Lee, W. S. V.; Xue, J., Metal Organic framework derived carbon for ultrahigh power and long cyclic life aqueous Zn ion capacitor. *Nano Materials Science* **2019**, 2(2), 159-163.

40. Wu, S.; Chen, Y.; Jiao, T.; Zhou, J.; Cheng, J.; Liu, B.; Yang, S.; Zhang, K.; Zhang, W., An Aqueous Zn-Ion Hybrid Supercapacitor with High Energy Density and Ultrastability up to 80000 Cycles. *Advanced Energy Materials* **2019**, 9(47), 1902915.

41. Yu, P.; Zeng, Y.; Zeng, Y.; Dong, H.; Hu, H.; Liu, Y.; Zheng, M.; Xiao, Y.; Lu, X.; Liang, Y., Achieving high-energy-density and ultra-stable zinc-ion hybrid supercapacitors by engineering hierarchical porous carbon architecture. *Electrochimica Acta* **2019,** *327*, 134999.